Surface Studies of ß-1,3,5,7-Tetranitro-1,3,5,7-Tetrazoctane and Pentaerythritol Tetranitrate from Density Functional Tight-Binding Calculations and Implications on Crystal Shape

Singh, Himanshu
Negre, Christian Francisco Andres
Redondo, Antonio
Perriot, Romain

To be published in: Crystal Growth & Design

DOI to publisher's version: 10.1021/acs.cgd.3c01487

CRYSTAL GROWTH & DESIGN

pubs.acs.org/crystal

Article

Surface Studies of β-1,3,5,7-Tetranitro-1,3,5,7-Tetrazoctane and Pentaerythritol Tetranitrate from Density Functional Tight-Binding Calculations and Implications on Crystal Shape

Himanshu Singh,* Christian F. A. Negre,* Antonio Redondo, and Romain Perriot

Cite This: https://doi.org/10.1021/acs.cgd.3c01487

Read Online

ACCESS | Metrics & More | Article Recommendations | Supporting Information

ABSTRACT: We use density functional tight-binding (DFTB) theory to calculate the surface energies of two energetic crystals: monoclinic β-1,3,5,7-tetranitro-1,3,5,7-tetrazoctane (β-HMX) and tetragonal pentaerythritol tetranitrate (PETN). The results are then employed to determine crystal shapes using the Bravais–Friedel–Donnay–Harker, attachment energy, and surface energy models. We find that energy-based models yield predictions in good agreement with experimental observations. Additionally, we propose a simple model that reframes surface energy as a measure of the lost intermolecular interactions during the formation of a surface from the bulk. The model accurately captures the results from the DFTB calculations and enables us to explain and predict surface energies as a function of the local molecular environment.

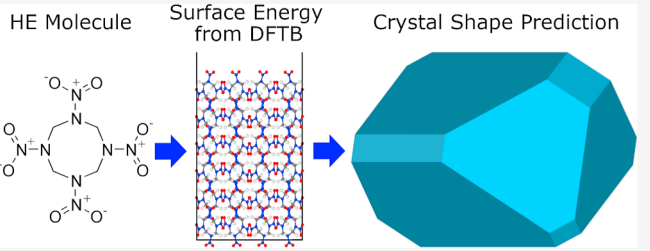

INTRODUCTION

Surface energy dictates many important properties of crystals, including surface reactivity, mechanical properties, growth rates, and equilibrium shape.[1−5] While this affects the behavior of many types of materials, from catalysts to pharmaceutical compounds, aspects related to crystal growth and shape are especially crucial for energetic materials (EMs), where microstructure directly impacts the response of an EM and therefore dictates performance and safety.[6,7] Understanding and predicting the surface properties of EMs such as β-1,3,5,7-tetranitro-1,3,5,7-tetrazoctane (β-HMX) and pentaerythritol tetranitrate (PETN), which are the focus of this article, are thus fundamental to controlling and tailoring their behavior. The structure of the β-HMX and PETN molecules is shown in Figure 1.

Experimental methods for measuring surface energy are generally based on contact angle measurements between a liquid droplet and the surface, assuming that the system is in thermodynamic equilibrium. However, this may not always be the case, especially if the droplet is evaporating or reacting with the surface.[8] Moreover, it is not always easy experimentally to cleave any crystal plane of interest,[9] and therefore, finding the surface energies of planes with kinks (the so-called "K" type planes) via experiments may be difficult.

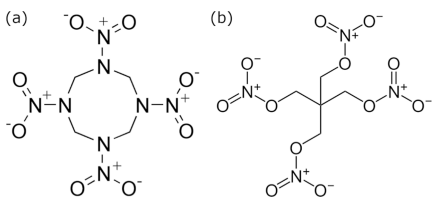

Figure 1. Chemical structures of (a) β-HMX and (b) PETN, employed in this study.

Atomistic simulations can be used to calculate surface energies and thus provide valuable information as long as the simulation method is accurate. The computational cost of density functional theory (DFT) can, however, be prohibitive for studying systems with thousands of atoms, which is often necessary to account for size effects.[10] Empirical models, on the other hand, do address the computational efficiency issue but may lack sufficient accuracy to provide meaningful results. For instance, different parametrizations and/or forms of the force field designed for a given material can lead to drastically different predictions from each other.[11,12]

In this work, we use density functional tight-binding (DFTB) theory, an approximate form of DFT,[13−15] to calculate the surface energies of various planes of β-HMX and PETN. DFTB provides accuracy approaching that of DFT. However, it is much faster than DFT, especially thanks to recent improvements leveraging GPU architectures,[16−18] allowing us to consider systems of several thousand atoms,

Received: December 13, 2023
Revised: March 28, 2024
Accepted: March 29, 2024

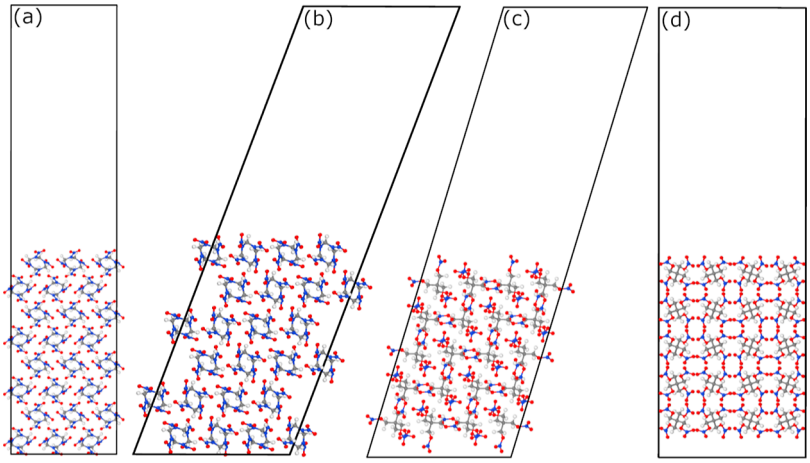

Figure 2. Simulation boxes for studying the planes (a) (010) of β-HMX, (b) (011) of β-HMX, (c) (011) of PETN, and (d) (110) of PETN. The corresponding box dimensions, in terms of lateral box vectors ($\boldsymbol{b} \times \boldsymbol{c}$), and the number of atoms are as follows: (a) 19.46 Å × 22.20 Å (2016 atoms), (b) 25.61 Å × 25.94 Å (2688 atoms), (c) 27.26 Å × 22.63 Å (1740 atoms), and (d) 20.21 Å × 25.70 Å (1740 atoms), respectively. All boxes are periodic in three dimensions. To prevent interaction between the two exposed surfaces, a sufficiently large vacuum space (≈50 Å) was introduced. Carbon (C), nitrogen (N), hydrogen (H), and oxygen (O) atoms are represented in gray, blue, white, and red colors, respectively.

i.e., sufficient to investigate crystal slabs. The *lanl*31 parametrization used in this work was shown to accurately reproduce the gas phase energy and configuration of organic molecules, as well as the principal Hugoniot of several high explosives (HEs).[19] As a result, it was used to reproduce energy barriers,[20] predict the reaction rate of nitromethane,[21] calculate the gas phase heat of formation of explosive molecules,[22] unravel the first reactions observed in shocked benzene[23] and during HE decomposition,[24] and predict the sensitivity of HEs.[25,26] Here, we apply it to surface energy studies.

Furthermore, we utilize the surface energies of the planes to predict the shapes of β-HMX and PETN through three established models: the geometry-based Bravais−Friedel−Donnay−Harker[27] (BFDH) model, the energy-based surface energy[28] (SE), and attachment energy[29] (AE) models. These models, based on the energetics and interplanar spacings of the planes, predict prominent planes and determine crystal shapes. As far as our knowledge goes, shapes from the SE and AE models are generally constructed by considering only a few selected planes, chosen based on whether the planes are found in experiments or possess large interplanar spacings.[30−35] This approach is susceptible to bias in the correct use of the models, and in this work, we have tried to remain as objective as possible in the selection of the planes included in the models.

While a study of surface energies cannot be exhaustive in the number of planes considered, the present study is, to the best of our knowledge, the most comprehensive produced so far and includes 25 planes, from the lower (100), (010), and (001) indices up to permutations of (210). Using these results, we find that crystal shapes from the SE and AE models are in good agreement with experimental observations, demonstrating the transferability of the *lanl*31 DFTB parametrization from gas-phase molecules to surface systems.

Lastly, we propose a neighbor shells model that relates surface energy to the atomistic environment of each molecule on the surface. The model accurately captures the results of the DFTB calculations and provides a simple explanation for the hierarchy of crystal surfaces based on the number of molecular interactions broken to create the bare surface from the bulk.

COMPUTATIONAL DETAILS

The DFTB calculations were performed within LAMMPS and the LATTE-LAMMPS interface,[36−38] using the *lanl*31 parametrization developed for CHNO compounds.[19] Additionally, long-range dispersion forces were accounted for via the pairwise correction presented in ref 39. ("*lanl*31 + D"), allowing us to reproduce the lattice parameters of the solid phases. All the calculations were run on A100 Nvidia's GPUs. PROGRESS[16,17] and BML[18] libraries were utilized to access GPU hardware and achieve enhanced performance.

Bulk systems for β-HMX and PETN were prepared from the Cambridge Structural Database[40] entries OCHTET13[41] and PERYTN12,[42] respectively. Equilibrium lattice parameters were obtained by relaxing 3 × 2 × 3 and 2 × 2 × 3 supercells for β-HMX and PETN (36 and 24 molecules), respectively. For monoclinic β-HMX, the lattice parameters a, b, c, and β were allowed to change independently, while the angles α and γ were constrained at 90°. For tetragonal PETN, the lattice parameters a, b, and c were allowed to change independently, while all three angles were constrained at 90°. The box relaxation problem is mathematically ill-defined,[43] so, in order to achieve convergence, iterations of conjugate gradient relaxation of the box and atoms and damped dynamics on the atoms alone were run until the tolerance of 0.001 eV and 0.3 bar were reached for the total energy and pressure, respectively.

Once the bulk system is relaxed, a crystal cutting tool (Los Alamos Crystal Cut, LCC[44]) was used to construct slabs in which the top and bottom faces expose the planes to be studied, as shown in Figure 2. The slabs are periodic in all three directions, but a vacuum gap of 50 Å was added above the surface of interest, which has been found to be sufficient to avoid an interaction between the system and its image. The thickness of the slab in the vertical direction is at least 5−6 molecular layers, and the dimensions in both lateral directions are at least 20 Å. In total, we have constructed surfaces for 25 planes, including those with lower indices, such as (001) up to the higher indices, such as (210).

The constructed slabs were then relaxed using the damped dynamics *fire* method[45] while keeping the box dimensions constant until the global force vector reached the tolerance of

https://doi.org/10.1021/acs.cgd.3c01487
Cryst. Growth Des. XXXX, XXX, XXX−XXX

Table 1. Comparison of the Lattice Parameters and Primitive Unit Cell Volume of β-HMX and PETN Obtained in This Work (*lanl*31 + D) with Experimental Results from Zhurova et al.[41,42a]

	method	a (Å)	b (Å)	c (Å)	β (deg)	V (Å^3)
β-HMX	exp	6.521	10.761	7.306	102.06	501.37
	*lanl*31 + D	6.486 (−0.5%)	10.453 (−2.9%)	7.400 (+1.3%)	101.92 (−0.1%)	490.83 (−2.1%)
	DFT + D	6.544 (+0.4%)	10.829 (+0.6%)	7.391 (+1.2%)	102.67 (+0.6%)	511.11 (+1.9%)
PETN	exp	9.276	9.276	6.613		568.97
	*lanl*31 + D	9.087 (−2.0%)	9.087 (−2.0%)	6.738 (+1.9%)		556.39 (−2.2%)
	DFT + D	9.401 (+1.3%)	9.401 (+1.3%)	6.554 (−0.9%)		579.19 (+1.8%)

[a]The experimental parameters for β-HMX are at 20 K,[41] and for PETN are at 100 K.[42] DFT + D results by Sorescu and Rice[46] are also included.

0.01 eV/Å. We find that this tolerance is sufficiently small for minimizing the total energy (refer to Figure S2 of the Supporting Information). The surface energy, γ^{hkl}, of the plane (hkl) was then calculated as

$$\gamma^{hkl} = \frac{E^{hkl} - ne^{bulk}}{2A^{hkl}} \quad (1)$$

where E^{hkl} is the energy of the slab, e^{bulk} is the energy of the bulk system per unit molecule, n is the number of molecules in the slab, and $2A^{hkl}$ is the area of the two exposed planes of the slab.

RESULTS

Bulk and Surface Energy Calculations. Table 1 displays the lattice parameters of bulk β-HMX and PETN obtained after relaxation, comparing them with values from experiments and prior DFT calculations.[41,42,46] The lattice parameters and primitive unit cell volume obtained with *lanl*31 + D agree remarkably well with the experimental results at low temperatures, showing a maximum difference of 2.9% for individual lattice constants and 2.2% for primitive unit cell volumes. DFT + D calculations by Sorescu and Rice achieved a similar level of accuracy, with maximum differences of 1.3% for lattice constants and 1.9% for primitive unit cell volumes, respectively.[46]

To investigate the convergence of surface energies with respect to slab thickness, we determined the surface energies of the (010) surface of β-HMX of varied slab thicknesses, as illustrated in Figure S3 of the Supporting Information. Based on these findings, all slabs examined in this study were constructed with a thickness of at least 5 molecular layers. It is noteworthy that an energy difference of 0.01 mJ/m^2 observed in the convergence study corresponds to 6.2 × 10^{-7} eV/Å^2 (less than 10^{-4} eV for a random 10 × 10 Å^2 unit cell surface), which falls below the bond energy for dispersion interactions.

Table 2 lists the surface energies of the studied planes in β-HMX and PETN, along with their interplanar spacings d^{hkl}. The planes (011) in β-HMX and (110) in PETN possess the lowest surface energies. Interestingly, these planes are also among the most prominent ones observed experimentally.[30,47] The space group for the PETN crystal is $P\bar{4}2_1c$, which dictates its structural equivalence along the directions of the two lattice vectors, $\boldsymbol{a}$ and $\boldsymbol{b}$. Due to this symmetry, the pairs of PETN planes (hkl) and (khl) are equivalent to each other. This symmetry is verified by the results shown in Table 2, where (hkl) and (khl) pairs in PETN are shown either to possess the same energy, as exemplified by the case of (011)/(101), or to exhibit nearly identical energies, as observed in (100)/(010) with a marginal difference of 0.58 mJ/m^2. The latter, for instance, is attributed to varying levels of convergence in the relaxation process.

Table 2. Surface Energy, γ^{hkl}, of Various Planes of β-HMX and PETN, Along with Their Interplanar Spacings, d^{hkl}[a]

β-HMX			PETN		
plane	γ^{hkl} (mJ/m^2)	d^{hkl} (Å)	plane	γ^{hkl} (mJ/m^2)	d^{hkl} (Å)
(011)	**86.54**	**5.95**	**(110)**	**71.85**	**6.43**
(01$\bar{1}$)	**87.30**	**5.95**	**(1$\bar{1}$0)**	**71.95**	**6.43**
(001)	101.91	7.24	(2$\bar{1}$0)	87.66	4.06
(01$\bar{2}$)	102.16	3.42	(210)	88.15	4.06
(012)	102.32	3.42	(120)	88.15	4.06
(021)	115.19	4.24	(1$\bar{2}$0)	88.19	4.06
(02$\bar{1}$)	115.20	4.24	(100)	94.67	9.09
(010)	**128.90**	**10.45**	(010)	95.25	9.09
(110)	**132.50**	**5.42**	**(011)**	**104.82**	**5.41**
(1$\bar{1}$0)	**132.87**	**5.42**	**(101)**	**104.82**	**5.41**
(120)	145.56	4.03	**(01$\bar{1}$)**	**104.88**	**5.41**
(1$\bar{2}$0)	145.75	4.03	**(10$\bar{1}$)**	**104.88**	**5.41**
(2$\bar{1}$0)	146.02	3.04	($\bar{1}$11)	108.89	4.65
(102)	146.21	2.90	(111)	109.04	4.65
(210)	146.82	3.04	(11$\bar{1}$)	109.06	4.65
(10$\bar{2}$)	148.93	3.47	(1$\bar{1}$1)	109.11	4.65
(101)	**150.87**	**4.35**	(201)	109.94	3.77
(1$\bar{1}$1)	155.15	4.01	(02$\bar{1}$)	109.94	3.77
(111)	155.31	4.01	(20$\bar{1}$)	109.98	3.77
(100)	155.57	6.35	(021)	109.98	3.77
(201)	159.32	2.71	(10$\bar{2}$)	124.13	3.16
(10$\bar{1}$)	**161.57**	**5.35**	(01$\bar{2}$)	124.63	3.16
(11$\bar{1}$)	163.48	4.76	(102)	124.66	3.16
($\bar{1}$11)	163.48	4.76	(012)	124.70	3.16
(20$\bar{1}$)	171.35	3.16	(001)	133.93	6.74

[a]The planes are sorted with respect to their surface energies, and those observed experimentally for β-HMX[47−49] and PETN[30,32,50−52] are highlighted in **bold**.

The bold indices in Table 2 represent planes of β-HMX and PETN observed in the experiments. It is interesting to note that the planes which have low surface energies or large interplanar spacings do not necessarily appear in the crystal shapes. In the discussion section, we show that the geometry of the planes is another factor which further governs the presence of certain planes in crystals.

Crystal Shape Models. Numerous shape prediction models have been developed to determine the crystal shapes. One of the simplest models, based solely on geometrical considerations, is the Bravais-Friedel-Donnay-Harker (BFDH) model. In this model, the distance (D^{hkl}) of each plane from the center of the crystal is inversely proportional to their interplanar spacings, i.e., $D^{hkl} \propto 1/d^{hkl}$.[27] The constant of proportionality can be set to any arbitrary value since it does

https://doi.org/10.1021/acs.cgd.3c01487
Cryst. Growth Des. XXXX, XXX, XXX−XXX

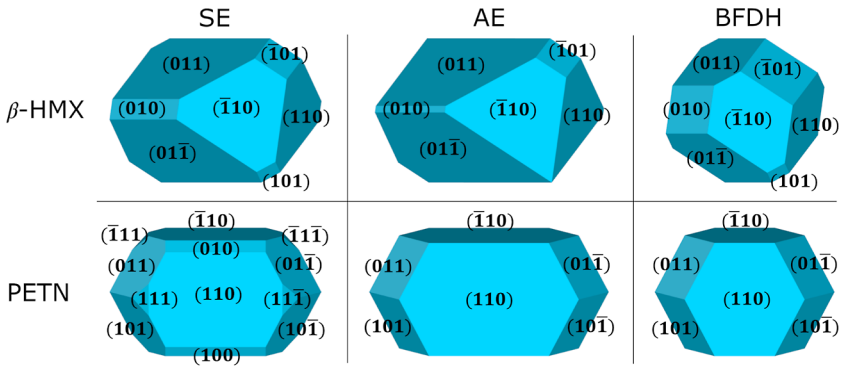

Figure 3. Prediction of the crystal shapes of β-HMX and PETN from the SE, AE, and BFDH models. In the BFDH[27] and AE[29] shapes of β-HMX, the interplanar spacing of (010) is effectively considered as $d^{020} = d^{010}/2$ [refer to Section S1 (plane extinction conditions) and Table S1 of the Supporting Information]. The rear faces of the shapes are symmetrically opposite to the front faces and share the same Miller indices but in the opposite direction.

not affect crystal shape prediction. A more refined model is the surface energy (SE) model, which posits that $D^{hkl} \propto \gamma^{hkl}$, where γ^{hkl} represents the surface energy (per unit area) of the planes.[28] Being an energy-based model, the SE model is expected to provide results in better agreement with experimental observations than the simpler BFDH model. Another energy-based model is the attachment energy (AE) model, developed by Hartman et al., in which $D^{hkl} \propto \gamma^{hkl} V/d^{hkl}$, with V being the volume of a primitive unit cell.[29] The AE of a plane is defined as the energy per molecule released when additional molecules crystallize on the plane.[29] It is expressed as $2\gamma^{hkl}V/(Zd^{hkl})$, where V/d^{hkl} represents the plane's reticular area, Z is the number of molecules in a primitive unit cell, and the factor 2 accounts for the pairwise interactions.[29] It is to be noted that units of each of the models are different, and therefore, the constants of proportionality in each of the models carry distinct units. Among these models, the SE model is known to provide equilibrium shapes, whereas the BFDH and AE models provide growth shapes.[31,53] In general, most crystals do not retain their equilibrium shape as they grow but instead follow nonequilibrium growth kinetics.[53] In such cases, the AE model is considered to be the most preferred for predicting crystal shapes.

The solvents may also significantly alter crystal shapes if they exhibit a preferential adsorption tendency on the crystal faces.[31,54,55] A modified AE model is, therefore, considered a better representative for predicting crystal shapes that account for solvent effects.[33,48,56−60] In the current scope of this work, we confine ourselves to predicting crystal shapes by using the BFDH, SE, and AE models. We have utilized the results presented in Table 2 and predicted the shapes of β-HMX and PETN, as shown in Figure 3. It is important to note that the interplanar spacing of certain planes is effectively reduced before being utilized in the expressions of the BFDH[27] and AE[29] models. The reduction of interplanar spacing for a given plane is considered when there exists another plane that is both parallel and structurally equivalent to it.[31,61] For instance, in β-HMX, an equivalent plane (020) exists for (010). Therefore, in the BFDH and AE models, we consider $d^{020} = d^{010}/2$ instead of d^{010}. Detailed information on the reduction in interplanar spacing and the planes for which reduced interplanar spacings are considered can be found in Section S1 (plane extinction conditions) and Table S1, respectively, of the Supporting Information.

From Figure 3, we observe that the same faces dominate in each model—(011), (01$\bar{1}$), ($\bar{1}$10), (110), ($\bar{1}$01), (010) for β-HMX, and (110), ($\bar{1}$10), (011), (101), (01$\bar{1}$), (10$\bar{1}$) for PETN. In the case of β-HMX, the shapes from the SE and AE models are nearly identical, except for the presence of (101) in the SE model, albeit with a small relative representation. The BFDH prediction is also qualitatively close to the energy-based models' predictions, displaying the same planes as the SE prediction but yielding a more isotropic crystal. For PETN, all three models provide similar shape predictions. The SE model has a marginal appearance of (010), (100), (111), (11$\bar{1}$), ($\bar{1}$11), ($\bar{1}$11$\bar{1}$), which are absent in the AE and BFDH models. The AE model predicts a more elongated shape than the SE model, while the BFDH model gives a more isotropic shape, as observed in the case of β-HMX. A detailed comparison of the shapes obtained for the two crystals with prior experimental observations is provided in the Discussion section.

Neighbor Shells Model. Here, we propose a simple model based on pairwise interactions between neighboring molecules to gain a better understanding of what determines whether a surface presents high or low energy. In this framework, a molecule in the bulk would have an energy $e^{\text{bulk}} = e^{\text{intra}} + \frac{1}{2}\sum_j (n_j^{\text{bulk}} \varepsilon_j)$, where e^{intra} represents the intramolecular energy of the molecule, and n_j^{bulk} is the number of jth nearest neighbors of the molecule, each interacting with the molecule with an energy of ε_j. The total energy of a bulk system would then be obtained by summing e_{bulk} over all molecules, i.e., $E^{\text{bulk}} = Ne^{\text{bulk}}$. When creating a surface, some of these interactions are lost (see Figure 4), and the energy of the slab is now

$$E^{hkl} = Ne^{\text{intra}} + \frac{1}{2}\sum_{i=1}^{N}\sum_{j}(n_{ij}^{hkl}\varepsilon_j) \tag{2}$$

where n_{ij}^{hkl} is the number of jth nearest neighbors of molecule i in the slab. Equation 2 thus provides a simple way of reframing slab energies, as long as (i) the molecules do not relax significantly at the surface (which would affect their internal energy e^{intra}); and (ii) we ignore interactions beyond pairs (manybody effects). While these constraints are important, we demonstrate below that the model is refined enough to reproduce surface energies with good accuracy.

The term "jth nearest neighbor" refers to a molecule positioned at the jth distance from the reference molecule, i.e.,

https://doi.org/10.1021/acs.cgd.3c01487
Cryst. Growth Des. XXXX, XXX, XXX−XXX

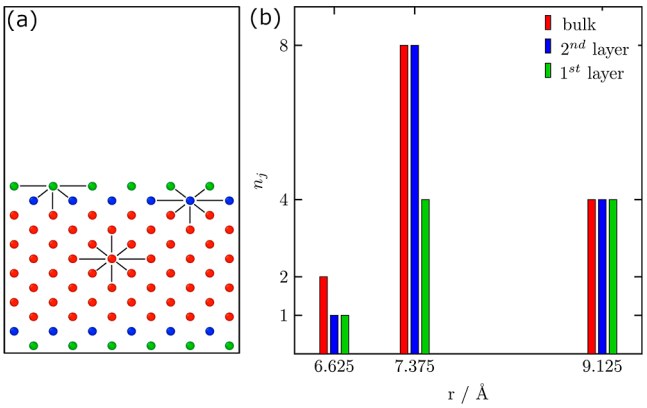

Figure 4. (a) Schematic of the (001) PETN slab, where red, blue, and green beads signify the center-of-mass of PETN molecules in the bulk, subsurface (second layer), and surface (first layer), respectively. (b) Histograms illustrating the number of nearest neighbors, n_j, for molecules in the bulk, second layer, and first layer of the (001) PETN slab. The 2D representation of nearest neighbors for each of these molecule types is shown via connecting lines in (a). The histograms reveal that, compared to the bulk molecules, those in the second layer lack only 1 neighbor at r = 6.625 Å, while those in the first layer also lack 4 neighbors at r = 7.375 Å. The neighbors are counted by calculating the radial distribution function around the reference molecules with a bin size of δr = 0.25 Å. We find that this bin size is sufficiently small to capture all the distinct kinds of neighbors.

in the jth neighbor shell. Crystal symmetry operations, as evident from the space groups ($P12_1/n1$ for β-HMX and $P\bar{4}2_1c$ for PETN), indicate that molecules situated at the same distance from the reference molecule are equivalent in terms of orientations. Therefore, we do not need to distinguish among several neighbors in shell j. The number of neighbors per shell, n_j^{bulk} and n_{ij}^{hkl}, can be determined by calculating the radial distribution function around the reference molecules in the bulk system and slab system, respectively. Figure 4 depicts, for instance, n_{ij}^{001} for three reference molecules of the (001) slab of PETN up to a radial distance of r < 10.5 Å. In Figure S4 of the Supporting Information, we show n_j^{bulk} for β-HMX and PETN within r < 10.5 Å. Within this cutoff, we obtain six distinct neighbor shells for β-HMX bulk molecules and three for PETN. We observed that interactions of reference molecules with neighbors lying beyond this distance are sufficiently negligible to be disregarded (details in the Discussion section).

Using eqs 1 and 2, the surface energy (per unit area) can now be expressed as

$$\gamma_{\text{model}}^{hkl} = -\frac{1}{4A^{hkl}} \sum_j [(N n_j^{\text{bulk}} - \sum_{i=1}^{N} n_{ij}^{hkl})\varepsilon_j] \quad (3)$$

where $\frac{1}{2A^{hkl}}(N n_j^{bulk} - \sum_{i=1}^{N} n_{ij}^{hkl})$ represents the number of jth nearest neighbors lost per unit surface area of (hkl) (see Figure S5 of the Supporting Information).

In order to determine the interaction terms ε_j within this pairwise model, we expressed the surface energy for each of the 25 planes according to eq 3 and minimized the cost function χ

$$\chi = \sum_{hkl} \left(\frac{\gamma_{\text{model}}^{hkl} - \gamma^{hkl}}{\gamma^{hkl}} \right)^2 \quad (4)$$

where γ_{hkl} is the surface energy obtained from the DFTB calculations. The values of ε_j obtained from this optimization process are presented in Table 3. The small values of ε_6 for β-HMX and ε_3 for PETN indicate that a model with six and three shells, respectively, is sufficient for each crystal. The neighbor shells model performs remarkably well, with an average error in the estimated surface energies below 3% for both crystals (see Figure 5, and Table S2 of the Supporting Information). Although some of the ordering differs, this model provides a simple way to estimate the hierarchy of different surface energies by measuring the lost intermolecular interactions. A more detailed analysis of the intermolecular interactions is given in Table S3 of the Supporting Information, where it is shown that the dominant intermolecular interactions arise from the dipole−dipole interactions between the polar nitro groups.

Table 3. Optimal Values of ε_j (eV) for the Two Crystals, Minimizing the Cost Function Defined in eq 4[a]

	β-HMX	PETN
ε_1	−0.489	−0.294
ε_2	−0.284	−0.184
ε_3	−0.187	−0.002
ε_4	−0.083	
ε_5	0.097	
ε_6	0.004	

[a]The notably small values of ε_6 = 0.004 eV for β-HMX and ε_3 = −0.002 eV for PETN suggest that interactions beyond sixth and third nearest neighbors, respectively, are negligible and can be ignored.

Additionally, we utilized surface energies obtained from the neighbor shells model to predict the shapes of both crystals (refer to Figure S6 of the Supporting Information). As anticipated, we observed a good match between the predicted shapes and those derived from DFTB energies. In β-HMX, a larger exposure of the ($10\bar{1}$) plane than that in the DFTB shapes (Figure 3) is attributed to the underestimation of its surface energy by −8.9% (see Table S2 of the Supporting Information). Similarly, the absence of planes (010), (100), (111), ($11\bar{1}$), ($\bar{1}11$), and ($\bar{1}1\bar{1}$), which marginally appeared in the DFTB shape of the SE model, results from the overestimation of their surface energies by +1.9 to +4.7%.

DISCUSSION

Our predictions of crystal shapes can be compared with available experimental results. Remarkably, the shapes of β-HMX crystals predicted from the SE and AE models closely match experimental observations reported by Yan et al.,[48] Gallagher et al.,[47] and Olokun et al.[49] (see Figure 6). To recall, the shape predictions of β-HMX from the SE and AE models are very similar, except that the plane ($\bar{1}0\bar{1}$) does not appear in the AE model, and the exposure of plane (010) is noticeably lesser in the AE shape.

Gallagher et al. and Olokun et al. employed the solvent evaporation method in acetone, obtaining β-HMX crystals of different shapes.[47,49] On the other hand, Yan et al. grew the crystals via the solvent cooling method in acetonitrile solvent and obtained only one shape of the crystal.[48] Interestingly, a crystal shape exists in all three methods, and this same crystal closely resembles our SE/AE models.

Figure 7 shows a comparison of our PETN shapes with the experiments. The experimentally obtained PETN crystals

https://doi.org/10.1021/acs.cgd.3c01487
Cryst. Growth Des. XXXX, XXX, XXX−XXX

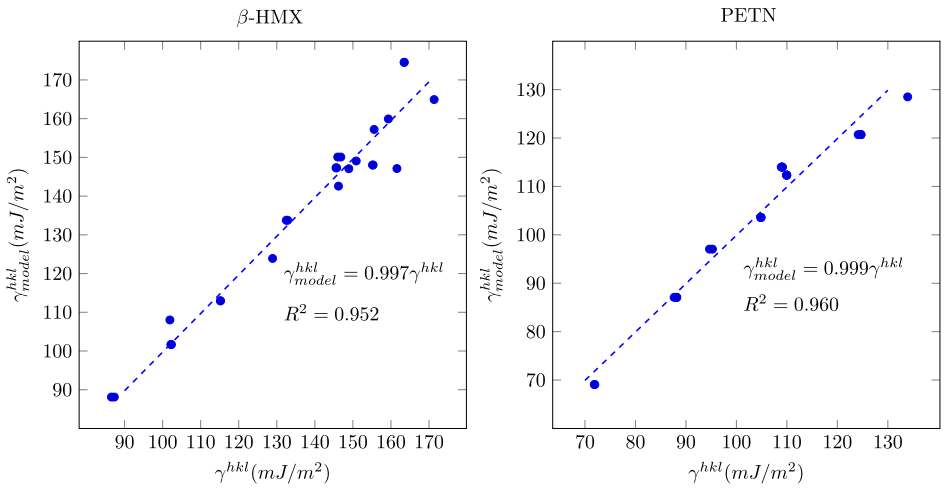

Figure 5. Comparison of surface energies calculated using the neighbor shells model ($\gamma^{hkl}_{\text{model}}$) and the corresponding DFTB values (γ^{hkl}) for 25 crystal planes in β-HMX and PETN. In the case of PETN, a significantly smaller number of data points are visible due to overlap among data points for different planes (refer to Table 2, and Table S2 of Supporting Information). The coefficients of determination, R^2, for both best-fit lines are close to 1, validating our model's ability to predict DFTB surface energies.

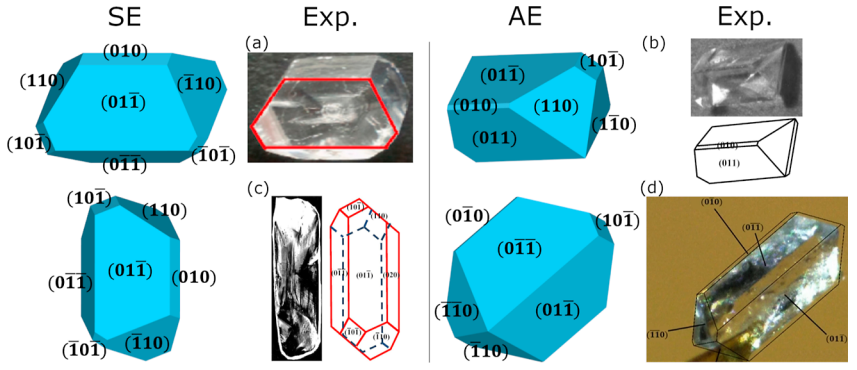

Figure 6. Comparison of predicted crystal shapes of β-HMX from SE and AE models with experimental observations. The theoretical shapes are identical to those presented in Figure 3 and are merely oriented differently to align with the experimental shapes. Notably, the shapes in the left panel exhibit the presence of $(\bar{1}0\bar{1})$ and a broader exposure of (010) compared to the shapes in the right panel. (a) is reprinted from ref 48, Copyright (2015), and (b) and (c) are reprinted from ref 47, Copyright (2017), with permissions from Elsevier. (d) is reprinted with permission under a Creative Commons CC BY 4.0 from ref 49, Copyright (2021), Springer Nature.

exhibit primary faces with (110) and $(\bar{1}10)$, and caps with (011), (101), $(01\bar{1})$, and $(10\bar{1})$. Shapes (a), (b), (c), and (d) are tabular, while shapes (e), (f), and (g) are elongated. It is noteworthy that all three shape prediction models effectively reproduce the tabular form of the PETN crystals. With the exception of the marginal appearance of (100), (010), (111), $(11\bar{1})$,$(\bar{1}11)$, and $(\bar{1}1\bar{1})$ in the SE model, all experimental planes are prominently captured in the predictions. Crystals in (a), (b), (c), (e), and (g) are formed in acetone solvent at low temperatures (~4 °C for (a), (e), and ~25 °C for (b), (c), (g)), and the one in (d) is formed in ethyl acetate at ~25 °C.[32,50−52,62] The elongation in (f) is attributed to non-equilibrium growth kinetics resulting from the aging of PETN crystals at elevated temperature (~80 °C) for 90 days.[32] However, the reasons for elongation in (e) and (g) are difficult to articulate based on the provided conditions.

To better quantify the prominence of planes in the predicted crystal shapes, we determined the area fractions of the planes forming these shapes (see Table 4). It is noteworthy that, out of the 25 planes considered in the shape prediction models, only 6 planes emerge prominently, and these align with those observed experimentally. Interestingly, these planes do not necessarily exhibit low γ^{hkl} or large d^{hkl} values (refer to Table 1); nevertheless, they stand out prominently and maintain correct proportions with respect to experimental observations. This results in an overall effective shape prediction, particularly evident in the SE and AE models. The reason behind this lies in the low Miller indices of these planes, making them geometrically less steep and, consequently, dominant over planes with larger Miller indices.[63] It is, therefore, the combined contributions from the surface energies and the geometry of the planes that determine the overall crystal shapes.

Lastly, an important quantity relevant to each plane is its roughness, which is, for instance, used to calculate solvent accessible surface area for predicting crystal shapes in different solvents.[33,48,56−60] In addition, roughness values can serve as criteria for down-selecting planes for use in theoretical shape prediction models. In cases where calculating surface energy for several planes is not feasible, down-selection is a common workaround to selectively provide planes to the models.[30−35]

Assuming that a rough (i.e., less flat) surface could be unfavorable for epitaxial growth, one may use this metric to select planes with only low roughness values. Therefore, we

https://doi.org/10.1021/acs.cgd.3c01487
Cryst. Growth Des. XXXX, XXX, XXX−XXX

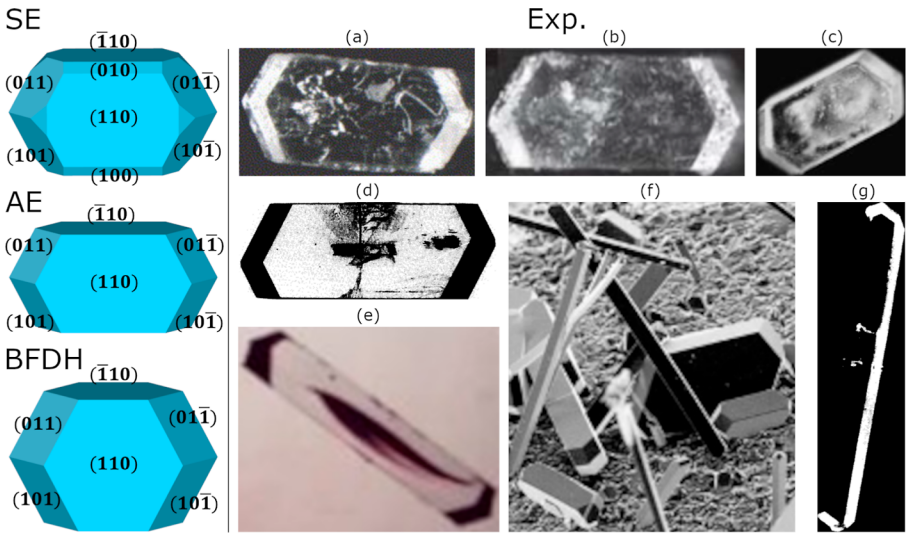

Figure 7. Comparison of predicted PETN crystal shapes from our models with experimental observations. The SE model predicts an equant shape, showcasing all experimental planes prominently. In contrast, the AE model predicts an acicular shape, emphasizing the key planes, except for the presence of (001) on the caps, which is not generally observed in the experiments. In the SE shape, the planes (111), (11$\bar{1}$), ($\bar{1}$11) , and ($\bar{1}$1$\bar{1}$)marginally appear and are therefore not labeled for clarity. (a) and (f) are reprinted from ref 32, Copyright (2006), and (d) and (g) are reprinted from ref 52, Copyright (1984), with permissions from Elsevier. (b) is reprinted from ref 50, Copyright (2007), with permission from Springer Nature. (c) is reprinted from ref 51, Copyright (2010), and (e) is reprinted from ref 62, Copyright (2016), with permissions from John Wiley & Sons.

Table 4. Area Fraction of Planes in the Predicted Crystal Shapes of β-HMX and PETN, Expressed as a Percentage[a]

β-HMX area fraction (%)				PETN area fraction (%)			
plane	SE	AE	BFDH	plane	SE	AE	BFDH
(011)	**31.6**	**34.5**	**21.8**	**(110)**	**27.2**	**25.6**	**27.9**
(01$\bar{1}$)	**31.6**	**34.5**	**21.8**	**(1$\bar{1}$0)**	**27.2**	**25.6**	**27.9**
(110)	**14.5**	**13.7**	**17.0**	**(011)**	**8.8**	**12.2**	**11.0**
(1$\bar{1}$0)	**14.5**	**13.7**	**17.0**	**(101)**	**8.8**	**12.2**	**11.0**
(010)	**4.2**	**1.3**	**9.6**	**(01$\bar{1}$)**	**8.8**	**12.2**	**11.0**
(10$\bar{1}$)	**2.7**	**2.2**	**11.5**	**(10$\bar{1}$)**	**8.8**	**12.2**	**11.0**
(101)	**0.8**	**0**	**1.2**	(100)	3.5	0	0
(10$\bar{2}$)	0	0	0	(010)	3.5	0	0
(001)	0	0	0	(111)	0.9	0	0
(01$\bar{2}$)	0	0	0	(11$\bar{1}$)	0.9	0	0
(012)	0	0	0	($\bar{1}$11)	0.9	0	0
(1$\bar{2}$0)	0	0	0	(1$\bar{1}$1)	0.9	0	0
(2$\bar{1}$0)	0	0	0	(001)	0	0	0
(102)	0	0	0	(210)	0	0	0
(210)	0	0	0	(120)	0	0	0
(120)	0	0	0	(1$\bar{2}$0)	0	0	0
(021)	0	0	0	(201)	0	0	0
(1$\bar{1}$1)	0	0	0	(02$\bar{1}$)	0	0	0
(111)	0	0	0	(20$\bar{1}$)	0	0	0
(100)	0	0	0	(021)	0	0	0
(201)	0	0	0	(10$\bar{2}$)	0	0	0
(02$\bar{1}$)	0	0	0	(01$\bar{2}$)	0	0	0
(11$\bar{1}$)	0	0	0	(102)	0	0	0
($\bar{1}$11)	0	0	0	(012)	0	0	0
(20$\bar{1}$)	0	0	0	(2$\bar{1}$0)	0	0	0

[a]The planes are sorted based on their area fractions in the SE shapes, with experimentally observed planes highlighted in **bold**. A clear match between the dominant planes found in the experiments and the SE/AE models is evident.

calculated the surface roughness of the planes of β-HMX and PETN by discretizing the region around the surface and computing the material density contribution via a Gaussian function centered around the atoms[64] (refer to Section S2 and Table S4 of the Supporting Information). Interestingly, we observed that planes with low roughness align very well with those observed in the experiments. The roughness values of 1.07 and 1.17 serve as natural cutoffs for β-HMX and PETN, respectively.

While our SE and AE models produced accurate predictions without limiting the planes, the prediction of β-HMX from the BFDH model showed significant variations in the proportions of exposed planes compared to the experiments. This is mainly due to the presence of (10$\bar{1}$) in the BFDH shape, which contributes a considerably larger exposed area (11.5%) than the energy models (2−3%) and the experiments (refer to Table 4).[47−49] It is noteworthy that the natural roughness cutoff for β-HMX clearly eliminates the plane (10$\bar{1}$) while retaining other planes within the cutoff. With the exclusion of (10$\bar{1}$), the resulting BFDH prediction yields a shape that aligns very well with the prismatic shape obtained by Lei et al.[57] (refer to Figure 8). Although our BFDH shape for PETN already resembles the experimental shapes, it is interesting to note that the prominent planes clearly fall within the natural roughness cutoff of 1.17.

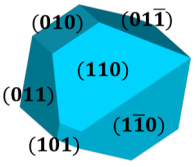

Figure 8. Modified BFDH shape of β-HMX obtained using planes with roughness up to 1.07 (refer to Table S4 of the Supporting Information). The shape matches very well with an experimental shape reported in refs 57 and 58.

https://doi.org/10.1021/acs.cgd.3c01487
Cryst. Growth Des. XXXX, XXX, XXX−XXX

CONCLUSIONS

We used DFTB simulations to calculate the surface energy of 25 planes of β-HMX and PETN. The results were then used to predict crystal shapes, which compare well with experimental observations. We also proposed a simple neighbor shells model that allows us to explain surface energy hierarchy based on the number of intermolecular interactions lost during the formation of the surfaces from the bulk and estimate surface energies of planes not considered in the study. This work demonstrates the transferability of the DFTB *lanl*31 parametrization from organic molecules in the liquid/gas phases to condensed phases. These results are an important step toward predicting a dynamic model of EM crystal growth.

ASSOCIATED CONTENT

Supporting Information

The Supporting Information is available free of charge at https://pubs.acs.org/doi/10.1021/acs.cgd.3c01487.

Plane extinction conditions; surface roughness calculation; surface profiles for the planes (001) and (101) of β-HMX; energy profiles for the slabs of (001) of β-HMX and (101) of PETN with respect to the number of energy minimization iterations using the damped dynamics fire method; surface energy of (010) of β-HMX as a function of slab thickness; histograms illustrating the number of nearest neighbors, n_j^{bulk}, for molecules in the bulk of β-HMX and PETN crystals; number of jth nearest neighbors lost per unit surface area upon creating slabs of β-HMX and PETN crystals; prediction of the crystal shapes by using the surface energies from the neighbor shells model; general and special reflection conditions of β-HMX and PETN crystals; calculation of surface energies for β-HMX and PETN crystals using the neighbor shells model; analysis of intermolecular interactions in the bulk β-HMX and PETN crystals calculated using DFTB (*lanl*31 + D); and surface roughness of planes in β-HMX and PETN crystals, organized by their roughness values (PDF)

AUTHOR INFORMATION

Corresponding Authors

Himanshu Singh − *Theoretical Division, Los Alamos National Laboratory, Los Alamos, New Mexico 87545, United States*; orcid.org/0000-0002-8437-686X; Email: himanshus@lanl.gov

Christian F. A. Negre − *Theoretical Division, Los Alamos National Laboratory, Los Alamos, New Mexico 87545, United States*; Email: cnegre@lanl.gov

Authors

Antonio Redondo − *Theoretical Division, Los Alamos National Laboratory, Los Alamos, New Mexico 87545, United States*

Romain Perriot − *Theoretical Division, Los Alamos National Laboratory, Los Alamos, New Mexico 87545, United States*; orcid.org/0000-0001-6131-1636

Complete contact information is available at: https://pubs.acs.org/10.1021/acs.cgd.3c01487

Notes

The authors declare no competing financial interest.

ACKNOWLEDGMENTS

This work was supported by the Laboratory Directed Research and Development program of Los Alamos National Laboratory under project no. 20220431ER. This research used resources provided by the Los Alamos National Laboratory Institutional Computing Program. Los Alamos National Laboratory is operated by Triad National Security, LLC, for the National Nuclear Security Administration of U.S. Department of Energy (contract no. 89233218CNA000001).

REFERENCES

(1) Tran, R.; Xu, Z.; Radhakrishnan, B.; Winston, D.; Sun, W.; Persson, K. A.; Ong, S. P. Surface Energies of Elemental Crystals. *Sci. Data* **2016**, *3*, 160080.

(2) Jiang, Q.; Lu, H.; Zhao, M. Modelling of Surface Energies of Elemental Crystals. *J. Phys.: Condens.Matter* **2004**, *16*, 521−530.

(3) Song, G.-L.; Mishra, R.; Xu, Z. Crystallographic Orientation and Electrochemical Activity of AZ31 Mg Alloy. *Electrochem. Commun.* **2010**, *12*, 1009−1012.

(4) Zhuang, H.; Tkalych, A. J.; Carter, E. A. Surface Energy as a Descriptor of Catalytic Activity. *J. Phys. Chem. B* **2016**, *120*, 23698−23706.

(5) Shariare, M. H.; Leusen, F. J.; de Matas, M.; York, P.; Anwar, J. Prediction of the Mechanical Behaviour of Crystalline Solids. *Pharm. Res.* **2012**, *29*, 319−331.

(6) Handley, C. A.; Lambourn, B. D.; Whitworth, N. J.; James, H. R.; Belfield, W. J. Understanding the Shock and Detonation Response of High Explosives at the Continuum and Meso Scales. *Appl. Phys. Rev.* **2018**, *5*, 011303.

(7) Perry, W. L.; Clements, B.; Ma, X.; Mang, J. T. Relating Microstructure, Temperature, and Chemistry to Explosive Ignition and Shock Sensitivity. *Combust. Flame* **2018**, *190*, 171−176.

(8) Papakonstantinou, C.; Chen, H.; Bertola, V.; Amirfazli, A. Effect of Condensation on Surface Contact Angle. *Colloids Surf., A* **2022**, *632*, 127739.

(9) Vaknin, U.; Sherman, D.; Gorfman, S. Geometrical Prediction of Cleavage Planes in Crystal Structures. *IUCrJ* **2021**, *8*, 793−804.

(10) Kleis, J.; Greeley, J.; Romero, N.; Morozov, V.; Falsig, H.; Larsen, A. H.; Lu, J.; Mortensen, J. J.; Dułak, M.; Thygesen, K. S.; et al. Finite Size Effects in Chemical Bonding: From Small Clusters to Solids. *Catal. Lett.* **2011**, *141*, 1067−1071.

(11) Padilla Espinosa, I. M.; Jacobs, T. D.; Martini, A. Evaluation of Force Fields for Molecular Dynamics Simulations of Platinum in Bulk and Nanoparticle Forms. *J. Chem. Theory Comput.* **2021**, *17*, 4486−4498.

(12) Khalkhali, M.; Ma, X.; Zhang, H.; Liu, Q. Bulk and Surface Properties of Gypsum: A Comparison Between Classical Force Fields and Dispersion-Corrected DFT Calculations. *Comput. Mater. Sci.* **2019**, *164*, 8−16.

(13) Seifert, G.; Joswig, J.-O. Density-Functional Tight Binding—An Approximate Density-Functional Theory Method. *Wiley Interdiscip. Rev. Comput. Mol. Sci.* **2012**, *2*, 456−465.

(14) Elstner, M.; Seifert, G. Density Functional Tight Binding. *Philos. Trans. R. Soc., A* **2014**, *372*, 20120483.

(15) Gaus, M.; Cui, Q.; Elstner, M. Density Functional Tight Binding: Application to Organic and Biological Molecules. *Wiley Interdiscip. Rev. Comput. Mol. Sci.* **2014**, *4*, 49−61.

(16) openhub.net. The QMD-Progress Open Source Project on Open Hub. https://www.openhub.net/p/qmd-progress (accessed 2019-9-2).

(17) Mniszewski, S. M.; et al. Enabling Particle Applications for Exascale Computing Platforms. 2021, arXiv:2109.09056. https://arxiv.org/abs/2109.09056.

(18) Bock, N.; Negre, C. F. A.; Mniszewski, S. M.; Mohd-Yusof, J.; Aradi, B.; Fattebert, J.-L.; Osei-Kuffuor, D.; Germann, T. C.; Niklasson, A. M. N. The Basic Matrix Library (BML) for Quantum Chemistry. *J. Supercomput.* **2018**, *74*, 6201−6219.

(19) Cawkwell, M. J.; Perriot, R. Transferable Density Functional Tight Binding for Carbon, Hydrogen, Nitrogen, and Oxygen: Application to Shock Compression. *J. Chem. Phys.* **2019**, *150*, 024107.
(20) Perriot, R.; Negre, C. F. A.; McGrane, S. D.; Cawkwell, M. J. Density Functional Tight Binding Calculations for the Simulation of Shocked Nitromethane with LATTE-LAMMPS. *AIP Conf. Proc.* **2018**, *1979*, 050014.
(21) Perriot, R.; Cawkwell, M. J.; Martinez, E.; McGrane, S. D. Reaction Rates in Nitromethane under High Pressure from Density Functional Tight Binding Molecular Dynamics Simulations. *J. Phys. Chem. A* **2020**, *124*, 3314−3328.
(22) Cawkwell, M. J.; Burch, A. C.; Ferreira, S. R.; Lease, N.; Manner, V. W. Atom Equivalent Energies for the Rapid Estimation of the Heat of Formation of Explosive Molecules from Density Functional Tight Binding Theory. *J. Chem. Inf. Model.* **2021**, *61*, 3337−3347.
(23) Martínez, E.; Perriot, R.; Kober, E.; Bowlan, P.; Powell, M.; McGrane, S.; Cawkwell, M. Parallel Replica Dynamics Simulations of Reactions in Shock Compressed Liquid Benzene. *J. Chem. Phys.* **2019**, *150*, 244108.
(24) Cawkwell, M. J.; Kober, E. M.; Perriot, R.; Myers, T. W.; Manner, V. W. Molecular Dynamics Simulations of the First Reactions in Nitrate Ester-based Explosives. *AIP Conf. Proc.* **2018**, *1979*, 050005.
(25) Cawkwell, M. J.; Manner, V. W. Ranking the Drop-Weight Impact Sensitivity of Common Explosives Using Arrhenius Chemical Rates Computed from Quantum Molecular Dynamics Simulations. *J. Phys. Chem. A* **2020**, *124*, 74−81.
(26) Cawkwell, M. J.; Davis, J.; Lease, N.; Marrs, F. W.; Burch, A.; Ferreira, S.; Manner, V. W. Understanding Explosive Sensitivity with Effective Trigger Linkage Kinetics. *ACS Phys. Chem. Au* **2022**, *2*, 448−458.
(27) Donnay, J. H.; Harker, D. A New Law of Crystal Morphology Extending the Law of Bravais. *Am. Mineral.* **1937**, *22*, 446−467.
(28) Wulff, G. XXV. Zur Frage der Geschwindigkeit des Wachsthums und der Auflösung der Krystallflächen. *Z. Kristallogr. Cryst.* **1901**, *34*, 449−530.
(29) Hartman, P.; Bennema, P. The Attachment Energy as a Habit Controlling Factor: I. Theoretical Considerations. *J. Cryst. Growth* **1980**, *49*, 145−156.
(30) Ibrahim, S. F.; Pickering, J.; Ramachandran, V.; Roberts, K. J. Prediction of the Mechanical Deformation Properties of Organic Crystals Based Upon Their Crystallographic Structures: Case Studies of Pentaerythritol and Pentaerythritol Tetranitrate. *Pharm. Res.* **2022**, *39*, 3063−3078.
(31) Winn, D.; Doherty, M. F. Modeling Crystal Shapes of Organic Materials Grown from Solution. *AIChE J.* **2000**, *46*, 1348−1367.
(32) Zepeda-Ruiz, L. A.; Maiti, A.; Gee, R.; Gilmer, G. H.; Weeks, B. L. Size and Habit Evolution of PETN Crystals—A Lattice Monte Carlo Study. *J. Cryst. Growth* **2006**, *291*, 461−467.
(33) Liu, Y.; Niu, S.; Lai, W.; Yu, T.; Ma, Y.; Gao, H.; Zhao, F.; Ge, Z. Crystal Morphology Prediction of Energetic Materials Grown from Solution: Insights into the Accurate Calculation of Attachment Energies. *CrystEngComm* **2019**, *21*, 4910−4917.
(34) Brunsteiner, M.; Price, S. L. Morphologies of Organic Crystals: Sensitivity of Attachment Energy Predictions to the Model Intermolecular Potential. *Cryst. Growth Des.* **2001**, *1*, 447−453.
(35) Klitou, P.; Rosbottom, I.; Karde, V.; Heng, J. Y.; Simone, E. Relating Crystal Structure to Surface Properties: A Study on Quercetin Solid Forms. *Cryst. Growth Des.* **2022**, *22*, 6103−6113.
(36) Plimpton, S. LAMMPS Molecular Dynamics Simulator. https://lammps.sandia.gov/ (accessed 2021-4-12).
(37) Bock, N.; Cawkwell, M. J.; Coe, J. D.; Krishnapriyan, A.; Kroonblawd, M. P.; Lang, A.; Saez, E. M.; Mniszewski, S. M.; Negre, C. F. A.; Niklasson, A. M. N.; Sanville, E.; Wood, M. A.; Yang, P. LATTE. 2008. https://github.com/lanl/LATTE, accessed 06/01/2023.
(38) Negre, C. F. A.; Cawkwell, M. J.; Plimpton, S. LATTE-LAMMPS Interface. 2017. http://lammps.sandia.gov/doc/fix_latte.html, accessed 06/01/2023.
(39) Lease, N.; Klamborowski, L. M.; Perriot, R.; Cawkwell, M. J.; Manner, V. W. Identifying the Molecular Properties that Drive Explosive Sensitivity in a Series of Nitrate Esters. *J. Phys. Chem. Lett.* **2022**, *13*, 9422−9428.
(40) Groom, C. R.; Bruno, I. J.; Lightfoot, M. P.; Ward, S. C. The Cambridge Structural Database. *Acta Crystallogr., Sect. B: Struct. Sci., Cryst. Eng. Mater.* **2016**, *72*, 171−179.
(41) Zhurova, E. A.; Zhurov, V. V.; Pinkerton, A. A. Structure and Bonding in β-HMX-Characterization of a Trans-Annular N···N Interaction. *J. Am. Chem. Soc.* **2007**, *129*, 13887−13893.
(42) Zhurova, E. A.; Stash, A. I.; Tsirelson, V. G.; Zhurov, V. V.; Bartashevich, E. V.; Potemkin, V. A.; Pinkerton, A. A. Atoms-in-Molecules Study of Intra- and Intermolecular Bonding in the Pentaerythritol Tetranitrate Crystal. *J. Am. Chem. Soc.* **2006**, *128*, 14728−14734.
(43) Plimpton, S. Fixes. https://docs.lammps.org/fix_box_relax.html (accessed 2023-10-13).
(44) Negre, C. F.; Alvarado, A.; Singh, H.; Finkelstein, J.; Martinez, E.; Perriot, R. A Methodology to Generate Crystal-based Molecular Structures for Atomistic Simulations. *J. Phys.: Condens.Matter* **2023**, *35*, 225001.
(45) Bitzek, E.; Koskinen, P.; Gähler, F.; Moseler, M.; Gumbsch, P. Structural Relaxation Made Simple. *Phys. Rev. Lett.* **2006**, *97*, 170201.
(46) Sorescu, D. C.; Rice, B. M. Theoretical Predictions of Energetic Molecular Crystals at Ambient and Hydrostatic Compression Conditions Using Dispersion Corrections to Conventional Density Functionals (DFT-D). *J. Phys. Chem. C* **2010**, *114*, 6734−6748.
(47) Gallagher, H.; Sherwood, J.; Vrcelj, R. The growth and perfection of β-cyclotetramethylene-tetranitramine (HMX) studied by laboratory and synchrotron X-ray topography. *J. Cryst. Growth* **2017**, *475*, 192−201.
(48) Yan, T.; Wang, J.-H.; Liu, Y.-C.; Zhao, J.; Yuan, J.-M.; Guo, J.-H. Growth and Morphology of 1, 3, 5, 7-tetranitro-1, 3, 5, 7-tetraazacy-clooctane (HMX) Crystal. *J. Cryst. Growth* **2015**, *430*, 7−13.
(49) Olokun, A.; Dillard, T.; Dhiman, A.; Tomar, V. Experimental study of anisotropic constitutive behavior of β-HMX crystals via nanoindentation and small-scale dynamic impact. *SN Appl. Sci.* **2021**, *3*, 875.
(50) Pitchimani, R.; Zheng, W.; Simon, S.; Hope-Weeks, L.; Burnham, A.; Weeks, B. Thermodynamic Analysis of Pure and Impurity Doped Pentaerythritol Tetranitrate Crystals Grown at Room Temperature. *J. Therm. Anal. Calorim.* **2007**, *89*, 475−478.
(51) Zhang, G.; Bhattacharia, S.; Weeks, B. Effect of Zinc Doping on Pentaerythritol Tetranitrate Single Crystals. *Cryst. Res. Technol.* **2010**, *45*, 732−736.
(52) Halfpenny, P.; Roberts, K.; Sherwood, J. Dislocations in Energetic Materials: I. The Crystal Growth and Perfection of Pentaerythritol Tetranitrate (PETN). *J. Cryst. Growth* **1984**, *67*, 202−212.
(53) Dandekar, P.; Kuvadia, Z. B.; Doherty, M. F. Engineering Crystal Morphology. *Annu. Rev. Mater. Res.* **2013**, *43*, 359−386.
(54) Hartman, P. The Attachment Energy as a Habit Controlling Factor II. Application to Anthracene, Tin Tetraiodide and Orthorhombic Sulphur. *J. Cryst. Growth* **1980**, *49*, 157−165.
(55) Hartman, P. The Attachment Energy as a Habit Controlling Factor: III. Application to Corundum. *J. Cryst. Growth* **1980**, *49*, 166−170.
(56) Cheng, Y.; She, C.; Qiao, M.; Jin, S.; Chen, S.; Li, L.; Chen, K. Molecular dynamics simulation on the crystal morphology of β-HMX affected by binary and ternary solvent systems. *J. Cryst. Growth* **2022**, *598*, 126874.
(57) Lei, W.; Dong, C.; Hong-zhen, L.; Xiao-hui, D.; Yan-wu, Y. Crystal Morphology of β-HMX Under Eight Solvents System Using Molecular Dynamics Simulation and Experiment. *Chin. J. Energ. Mater.* **2020**, *28*, 317−329.

https://doi.org/10.1021/acs.cgd.3c01487
Cryst. Growth Des. XXXX, XXX, XXX−XXX

(58) Zhai, L.; Zhao, X.; Rui, J.; Qiu, S.; Li, Y. Molecular Dynamics Simulation of β-HMX Crystal Morphology Induced by Polymer Additives. *Crystals* **2022**, *12*, 164.
(59) Tao, J.; Wang, X. Crystal structure and morphology of β-HMX in acetone: A molecular dynamics simulation and experimental study. *J. Chem. Sci.* **2017**, *129*, 495−503.
(60) Duan, X.; Wei, C.; Liu, Y.; Pei, C. A Molecular Dynamics Simulation of Solvent Effects on the Crystal Morphology of HMX. *J. Hazard. Mater.* **2010**, *174*, 175−180.
(61) Aroyo, M. I. International Tables for Crystallography. *Vol. A: Space-Group Symmetry*; Springer, 2016.
(62) Zhai, M.; McKenna, G. B. Mechanical Properties of Pentaerythritol Tetranitrate (PETN) Single Crystals from Nano-Indentation: Depth Dependent Response at the Nano Meter Scale. *Cryst. Res. Technol.* **2016**, *51*, 414−427.
(63) Barmparis, G. D.; Lodziana, Z.; Lopez, N.; Remediakis, I. N. Nanoparticle Shapes by Using Wulff Constructions and First-Principles Calculations. *Beilstein J. Nanotechnol.* **2015**, *6*, 361−368.
(64) Willard, A. P.; Chandler, D. Instantaneous Liquid Interfaces. *J. Phys. Chem. B* **2010**, *114*, 1954−1958.

https://doi.org/10.1021/acs.cgd.3c01487
Cryst. Growth Des. XXXX, XXX, XXX−XXX